Single Nb atom modified anatase TiO_2(110) for efficient electrocatalytic nitrogen reduction reaction

Yunnan Gao,[a] *Yang Yang*,[a,b] *Leiduan Hao*,[a] *Song Hong*,[a] *Xinyi Tan*,[*c] *Tai-Sing Wu*,[d] *Yun-Liang Soo*,[e] *Alex W. Robertson*,[f] *Qi Yang,**,[a] *Zhenyu Sun**,[a]

[a] State Key Laboratory of Organic-Inorganic Composites, College of Chemical Engineering, Beijing University of Chemical Technology, Beijing 100029, P. R. China

[b] School of Materials, Sun Yat-sen University, Gongchang Road 66, Shenzhen, 510187, P. R. China

[c] Beijing, P. R. China

[d] National Synchrotron Radiation Research Center, Hsinchu 30076, Taiwan

[e] Department of Physics, National Tsing Hua University, Hsinchu 30013, Taiwan

[f] Department of Physics, University of Warwick, Coventry CV4 7AL, U. K.

KEYWORDS: N_2 reduction reaction; NH_3; Electrolysis; Density functional theory; Nb atoms; Anatase TiO_2

ABSTRACT: The electrochemical nitrogen reduction reaction (NRR) is an attractive alternative to the conventional Haber-Bosch process. However, the competitive hydrogen evolution reaction (HER), with faster reaction kinetics and lower overpotentials, causes severe energy efficiency loss during the NRR. To date, the informed design of tailored electrocatalysts that maintain good efficiency toward the NRR remains a challenge. Herein, we report the theory-guided design of anatase-supported Nb catalysts. Theoretical calculations predict that Nb atoms deliver multi-functional enhancement toward the NRR when incorporated in an anatase TiO_2(110) catalyst: (1) Decreasing the band gap and inducing electrons to promote the conductivity of TiO_2(110), (2) suppressing the undesired competitive HER, (3) activating the inert Ti sites for N_2 adsorption, (4)

enabling fast charge transfer between *NNH and the TiO_2(110) surface, and (5) reducing the energy barrier of the potential-determining *N_2 → *NNH step, further facilitating NH_3 formation. As a result, our Nb-TiO_2(110) catalyst exhibits superior activity and selectivity for the NRR, which affords an NH_3 production rate of about 21.3 μg h^{-1} mg_{cat}^{-1} and NH_3 faradaic efficiency of ~9.2% at −0.5 V (versus reversible hydrogen electrode). This study provides insights for the rational design of efficient electrocatalysts for the NRR.

1. INTRODUCTION

The century-old Haber-Bosch process is the major method for the production of ammonium fertilizer and other synthetic nitrogen compounds worldwide. Due to the chemically inert nature of N_2, with its extremely strong N≡N triple bond,[1,2] the Haber-Bosch process requires harsh reaction conditions (400−600 °C, 20−40 MPa) that consume 1−2% of the world's annual fossil energy output. This generates over 1.5 tons of CO_2 per ton of produced NH_3.[3,4] In this context, as a sustainable alternative[5,6] to the Haber-Bosch process, the electrochemical nitrogen reduction reaction (NRR) proceeding under ambient conditions has attracted growing research interest in recent years.[7,8]

The NRR ($N_2(g) + 6H^+ + 6e^- \leftrightarrow 2NH_4^+(aq.)$) normally consists of three steps:[9] 1) adsorption of N_2 molecules on the catalytic active sites, 2) cleavage of the N–N bonds and subsequent hydrogenation of N_2, 3) desorption of the as-formed NH_3 molecules from the catalyst surface. Unfortunately, the hydrogenation processes associated with multiple electron-transfer are often hampered by the hydrogen evolution reaction (HER), which incorporates only two electrons for H_2 formation[10] and competes with the NRR under similar redox potentials, thus inhibiting the NH_3 yield rate and faradaic efficiency (FE).[11,12] Great efforts have been devoted to improving the

performance of ammonia electrosynthesis by different strategies, including development of NRR-active species with inferior HER activity, or by regulation of the electronic structure of the electrocatalysts.[13,14]

TiO_2 has been considered as a promising NRR electrocatalyst since it is non-toxic, abundant, and has good chemical stability as well as poor activity toward the HER. Unfortunately, as a semiconductive semi-metal, unmodified TiO_2 displays low conductivity and weak adsorption and activation for N_2.[15,16] It has been reported that introducing oxygen vacancies (V_O)[17] and heteroatoms (e.g., V,[18] Fe,[19] Zr,[20] Cu,[21] and La[22]) can promote the NRR activity of TiO_2. Han et al. suggested that V_O are able to stabilize $*N_2$ and *NNH intermediates, thus improving NRR performance.[18] Surface Ti and V atoms in a V-doped TiO_2 facilitated the enhanced generation of $*NH_2NH_2$ intermediate.[19] Alongside compositional modification, taking advantage of the various surface electronic structures and energy band levels of the different crystal facets in TiO_2 is another useful strategy for boosting its catalytic activity.[23,24] A theoretical calculation predicted that the (110) surface of anatase TiO_2 has higher surface energy than both the (010) and (101) surfaces,[25] indicating that the (110) facets have greater potential for loading heteroatoms. According to the prior DFT study by Zhang et al.,[27] among the candidates of Pd, Pt ,Ni, Fe, Co, Mo, and V on the substrate of black phosphorus, Nb is the most efficient heteroatom to balance the rate-determining steps in NRR. This inspired us to explore the incorporation of Nb on TiO_2 for NRR.

In this work, we perform density functional theory (DFT) calculations that predict the cooperative effect of Nb and anatase TiO_2(110) in promoting electrocatalytic NRR performance. The Nb atoms dispersed on TiO_2(110) yield better conductivity with a more stable structure, compared to pristine TiO_2(110) and Nb-TiO_2(101). Guided by our theoretical calculations, we successfully synthesize TiO_2 single crystals with selectively exposed (110)

facets, supplemented with Nb atomic loading (denoted as Nb-TiO_2(110)). In 0.1 M Na_2SO_4 electrolyte, Nb-TiO_2(110) exhibited exceptional performance for NRR, achieving an NH_3 production rate of ~21.3 μg h^{-1} mg_{cat}^{-1} and NH_3 FE of ~9.2% at −0.5 V (versus reversible hydrogen electrode, *vs*. RHE).

2. RESULTS AND DISCUSSION

We first conducted DFT calculations on the optimized model structures in order to elucidate the electronic properties of Nb-TiO_2 structure. For comparison, the most stable (101) facets were also taken into account (Figure S1). For calculations with ideal (101) and (110) facets, Nb atoms were situated on the surface of TiO_2 such that they coordinated with three and five oxygen atoms, respectively (Figure 1A and B). The binding energy of Nb-TiO_2(101) and Nb-TiO_2(110) was calculated to be 2.04 and −0.46 eV, respectively, suggesting a stronger adsorption and interaction between Nb and the TiO_2(110) facet. Figure 1C shows the density of states (DOS) of pristine TiO_2(110), Nb-TiO_2(101), and Nb-TiO_2(110). Pristine TiO_2(110) is semiconducting with a 1.6 eV band gap at the Fermi level. Nb-TiO_2(101) presents a 0.2 eV band gap. However, no band gap was found for Nb-TiO_2(110), and the electron density on the Fermi level significantly increased, suggesting a much better electrical conductivity,[26] which is beneficial to the NRR kinetics due to promoting the proton-coupled electron-transfer process.[27]

The catalytic mechanisms of the NRR process on pristine TiO_2(101), pristine TiO_2(110), and Nb-TiO_2(110) were also explored through DFT calculations. We canvassed two typical NRR associative pathways, namely distal and alternating mechanisms, in which all possible reaction intermediates are involved (Figure S2). As shown in Figure 1D, and consistent with a previous study,[21] TiO_2(110) and Nb-TiO_2(110) prefer the alternating route instead of the distal route, while TiO_2(101) follows the distal route. Despite the different reaction routes, the three systems shared

the same step of protonation of $*N_2$ to form *NNH species (* denotes a surface site) as the potential-determining step (PDS). The limiting potential (ΔG_{PDS}) for TiO_2(110), Nb-TiO_2(110), and TiO_2(101) is 1.81, 1.64, and 1.91 eV, respectively, indicating that Nb-TiO_2(110) is most favorable for NRR.[28]

We also compared the HER activities of the catalysts. According to previous studies, an HER electrocatalyst can be qualitatively judged by the Gibbs free energy change of the first elementary step ($H^+ + e^- \rightarrow H^*$).[29] As shown in Figure 1E, the free energy change of H adsorption (ΔG(*H)) on TiO_2(101), TiO_2(110), and Nb-TiO_2(110) is −0.08, −0.22, and 0.61 eV, respectively, implying that HER is much easier on TiO_2(101) and TiO_2(110) than on Nb-TiO_2(110). It is worth noting that all the three catalysts exhibit exothermic N_2 adsorption, thus chemisorb N_2 molecules spontaneously. However, pristine TiO_2 can also adsorb H_2 spontaneously, yet for Nb-TiO_2(110) extra energy is needed to adsorb H_2. The net difference of $\Delta G(*N_2) - \Delta G$(*H) for Nb-$TiO_2$(110) (−0.98 eV) is much smaller than that for TiO_2(110) (0.04 eV) and TiO_2(101) (−0.09 eV), indicating that N_2 adsorption is less hindered by *H after Nb atom decoration.

To further investigate the reaction step of $*N_2 + H^+ + e^- \rightarrow$ *NNH, integrated-crystal orbital Hamilton population (ICOHP)[30] analysis of the N≡N bond was performed to investigate the activation degree for N_2 molecules, which was generally negatively correlated with the values of ICOHP. As shown in Figure 1F, Nb-TiO_2(110) exhibits less negative ICOHP (−17.59) with stronger activation for N≡N bond than pristine TiO_2(110) (−18.48). The charge density difference of the *NNH state configuration was calculated, as shown in Figure 1G. The electron transfer from Nb-TiO_2(110) to the *NNH intermediate (0.351 |e|) was higher than that from TiO_2(110) (0.013|e|), suggesting a stronger electron interaction between Nb-TiO_2(110) and the *NNH intermediate.[31]

Therefore, introducing Nb atoms to TiO_2(110) facets should improve the activation of $*N_2$ and promote charge transfer to form *NNH in the PDS, further facilitating the NRR.

Based on these theoretical predictions, it is reasonable to envision that Nb-TiO_2(110) has the potential to achieve a positive catalytic performance for the NRR. We next started experiments accordingly.

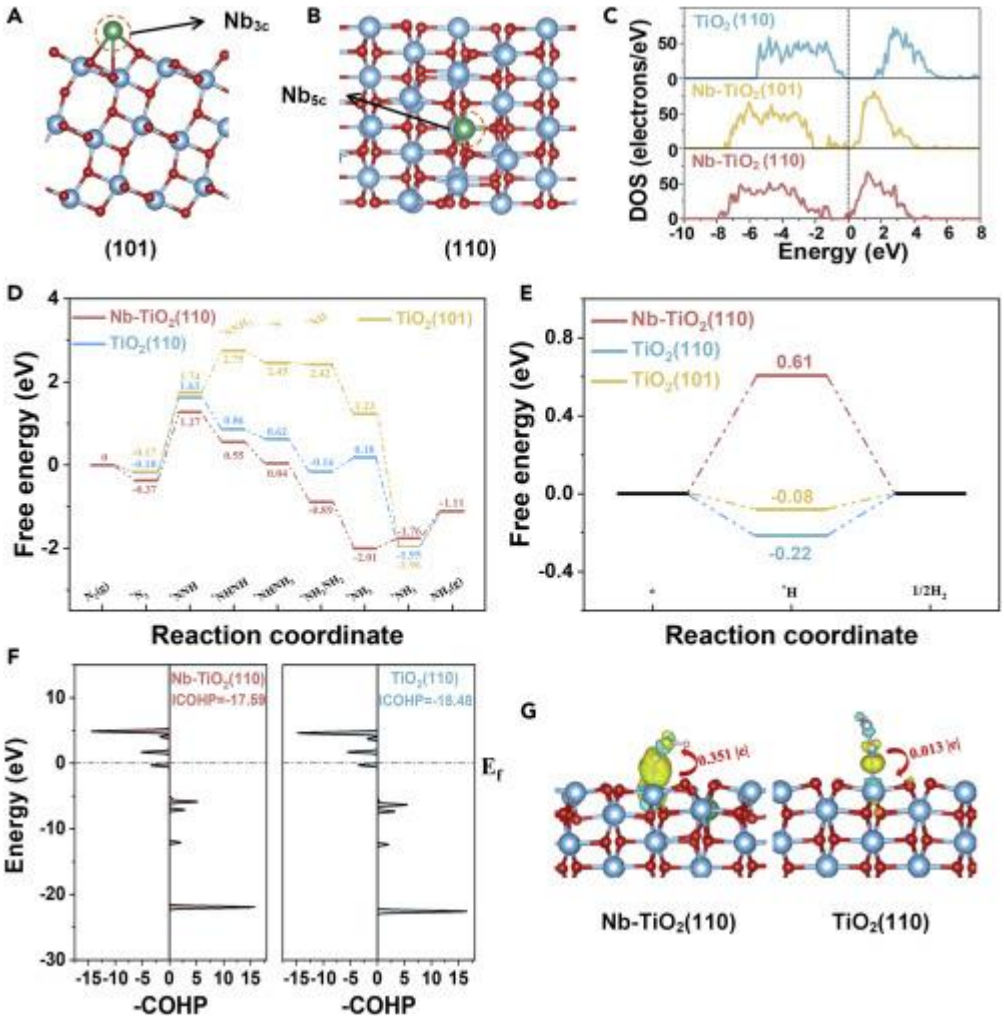

Figure 1. The surface structure of (A) Nb-TiO_2(101) and (B) Nb-TiO_2(110). (C) Projected density of states of TiO_2(110), Nb-TiO_2(101), and Nb-TiO_2(110). (D) The Gibbs free energy diagrams on the TiO_2(101), TiO_2(110), and Nb-TiO_2(110) along the respective optimum NRR reaction pathways. (E) The HER Gibbs free energy diagrams on the TiO_2(101), TiO_2(110), and Nb-

TiO_2(110). (F) The crystal orbital Hamilton population (COHP) between N–N bond of the adsorbed *NNH intermediates for pure TiO_2(110) and Nb-TiO_2(110), respectively. (G) Charge density difference of the *NNH intermediates for TiO_2(110) and Nb-TiO_2(110). Yellow and blue isosurface are demonstrated as positive and negative changes of density, respectively.

We synthesized Nb-TiO_2(110) via a simple one-step solvothermal strategy. The X-ray diffraction (XRD) pattern (Figure 2A) showed Nb-TiO_2(110) crystallized in the anatase TiO_2 phase (JCPDS no. 21−1272), and the (101) Bragg reflection shifted to a lower 2θ angle with the loading of Nb atoms to TiO_2 (inset of Figure 2A), indicating a change in structure due to doping. Nb was not detected by XRD due to its small particle size and/or low content, confirmed as 3.36 wt% loading by inductively coupled plasma optical emission spectrometry (ICP-OES) analysis (Figure S3). The surface atomic composition and the chemical state were investigated using X-ray photoelectron spectroscopy (XPS). The Nb 3d spectrum of Nb-TiO_2(110) exhibited two peaks at 206.9 and 209.6 eV (Figure 2B), which can be assigned to the binding energies of Nb^{5+} $3d_{5/2}$ and Nb^{5+} $3d_{3/2}$, respectively,[32] while no peak of Nb was detected for pristine TiO_2(110). The binding energies of Ti 2p at 464.3 and 458.6 eV (Figure 2C) indicated the existence of Ti^{4+} without other Ti species.[33] In addition, the peaks showed no shift after introducing Nb, demonstrating that Nb atoms did not change the chemical valences of Ti^{4+} ions, thus it was unlikely to have formed new Nb–Ti–O bonds. The N 1s XPS spectra confirmed the absence of N in the as-synthesized catalysts (Figure 2D). The O 1s peaks at 529.8 and 531.8 eV (Figure S4) are indicative of bonding between O and Ti in the form of Ti–O linkage for TiO_2[34] and the presence of –OH groups on the surface,[35] respectively. After the loading of Nb, a strong peak at 533.2 eV emerged, which resulted from the carboxyl group of niobium oxalate.[36]

The Raman peaks of pristine TiO_2(110) are observed at 149.8 cm^{-1} (E_g), 399.8 cm^{-1} (B_{1g}), 512.4 cm^{-1} (A_{1g}), and 634.5 cm^{-1} (E_g), corresponding to the anatase TiO_2 (Figures 2E and S5).[37,38] The band at 399.8 cm^{-1} slightly shifted to a higher wavenumber for Nb-TiO_2(110) due to the difference in size of the Nb and Ti ions, leading to a distortion of the TiO_2 lattice after loading of Nb atoms, supporting our XRD observation (Figure 2A). The Fourier transform infrared (FTIR) spectra exhibited an infrared absorption band at around 550 cm^{-1} for TiO_2, which shifted to 570 cm^{-1} for Nb-TiO_2(110) (Figure 2F). This band belongs to the bending and stretching vibration of Ti–O group (300–800 cm^{-1}),[39] with the shift further confirming the successful attachment of Nb on TiO_2.

To visualize the adsorption and activation of N_2 on the catalysts, N_2-temperature programmed desorption (N_2-TPD) was conducted (Figure 2G). Generally, the peak and the area of desorbed temperature represent adsorption strength and capacity of the gas, respectively.[40] For pristine TiO_2(110), only one N_2 desorption peak at 379 °C was observed. In contrast, Nb-TiO_2(110) displayed one N_2 physical adsorption peak at 287 °C and two N_2 chemisorption peaks at 366 and 579 °C, indicating that Nb-TiO_2(110) possesses two sites (Ti and Nb) for N_2 adsorption with significantly enhanced interaction between N_2 gas and the catalyst, which could bring advantageous activity for the NRR. The N_2 adsorption–desorption isotherms of TiO_2(110) and Nb-TiO_2(110) are depicted in Figure S6. A typical type II isotherm is observed based on the Brunauer–Deming–Deming–Teller classification, where the Brunauer–Emmett–Teller surface area of Nb-TiO_2(110) was estimated to be ~86.8 m^2 g^{-1}, larger than that of TiO_2(110) (~43.8 m^2 g^{-1}). High surface areas favor accessibility to reactants and also benefit mass transport of reactants and intermediates, conducive to improved catalytic activity.

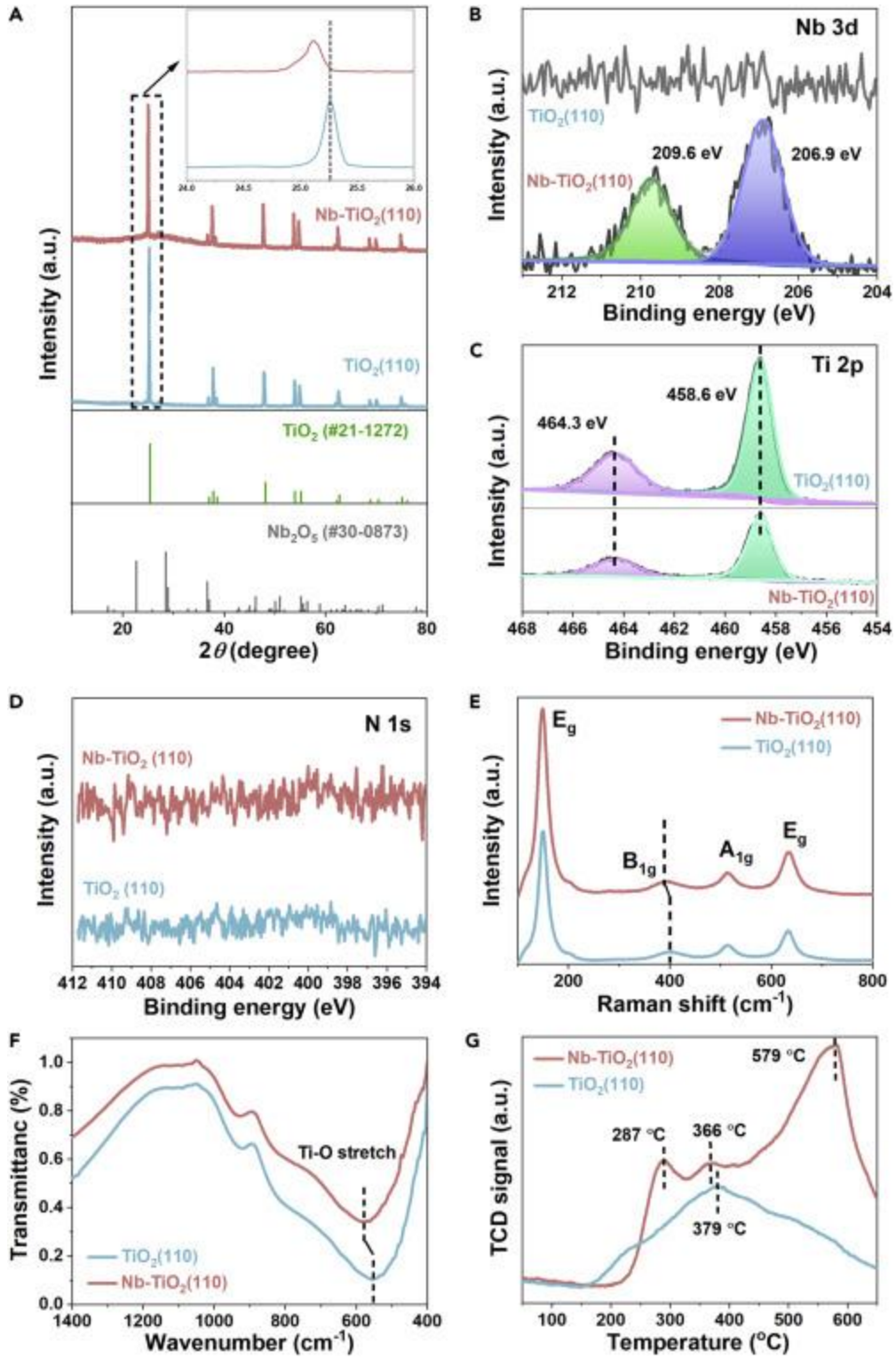

Figure 2. (A) XRD patterns, (B) Nb 3d, (C) Ti 2p and (D) N 1s XPS spectra, (E) Raman and (F) FTIR spectra, and (G) N_2-TPD results of TiO_2(110) and 3.36% Nb-TiO_2(110). The inset in (A) shows the magnified XRD pattern from the encased dashed square.

We further employed X-ray absorption fine structure (XAFS) measurements to probe the chemical environment of Nb in the as-made Nb-TiO_2(110). Figure 3A displays the Nb K-edge X-ray absorption near-edge structure (XANES) spectra of Nb-TiO_2(110) and reference samples of commercial Nb_2O_5 and Nb foil. As opposed to Nb foil, the Nb K-edges of Nb-TiO_2(110) shift to a higher energy and the average oxidation state of Nb in the sample is close to +5, in good agreement with the above-mentioned XPS results (Figure 2B). Figure 3B presents the Fourier transform (FT) k^3-weighted extended X-ray absorption fine structure (EXAFS) spectra of the three samples. The first-shell peak can be fitted well with a Nb–O coordination number of 4.7 ± 0.4 (~2.0 Å, Table S1), as well as a small Nb–Ti contribution (3.1 Å, Table S1). Note that the peak of Nb–Nb at *ca*. 2.61 Å is very weak (Figure 3C), implying the formation of isolated single Nb atoms. Since the EXAFS can only give an average coordination number, the result can be considered to be consistent with the Nb–O_5 coordination environment applied in the DFT models. This confirmed that the majority of Nb species in Nb-TiO_2(110) existed in the form of Nb–O_5 atoms.

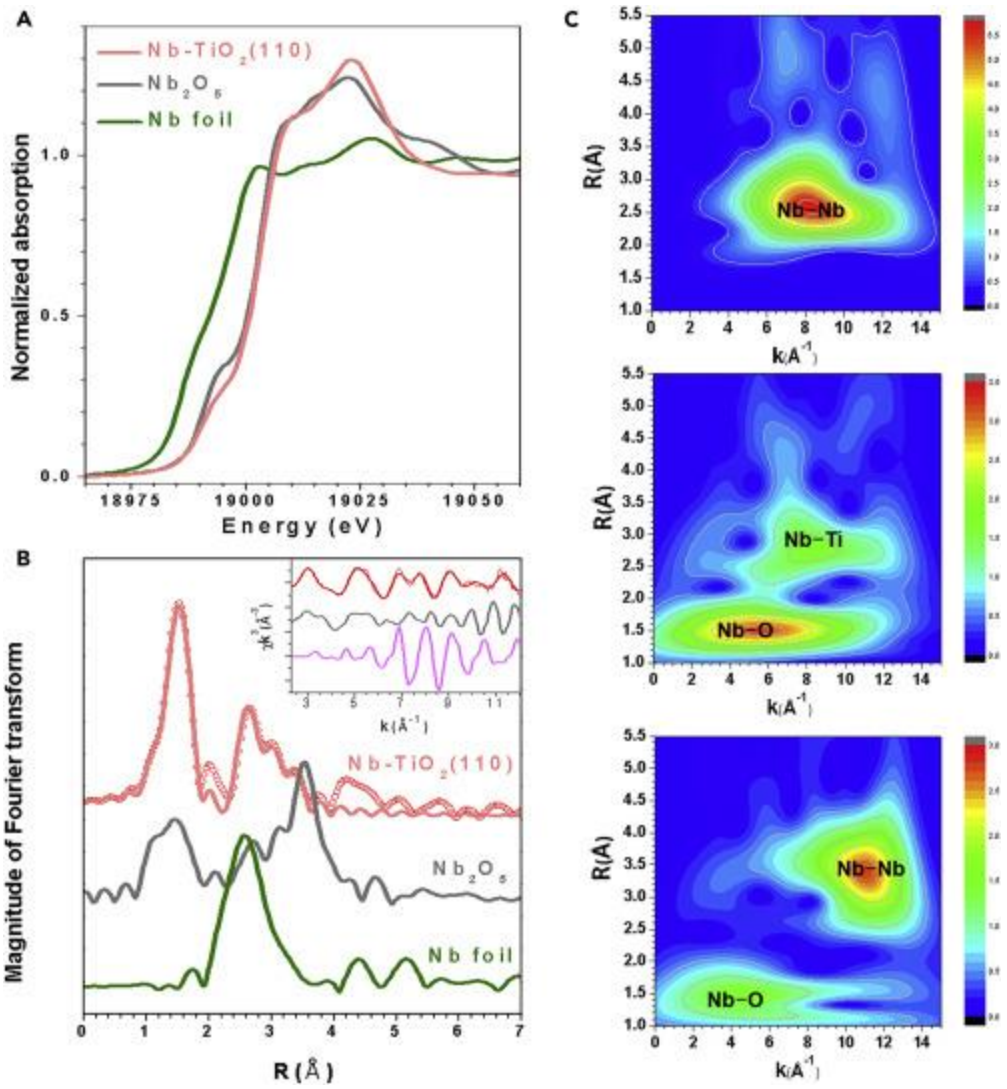

Figure 3. (A) Nb K-edge XANES spectra and (B) FT k^3-weighted EXAFS spectra in the R space of 3.36% Nb-TiO_2(110) along with those of Nb foil and Nb_2O_5 as reference standards. (C). Wavelet transform of the k^3-weighted EXAFS data of Nb foil, commercial Nb_2O_5, and 3.36% Nb-TiO_2(110).

Scanning electron microscopy (SEM) images of the as-prepared Nb-TiO_2(110) revealed the lateral size of the obtained Nb-TiO_2(110) is about 3–5 μm (Figure 4A), with the crystals exhibiting regular morphologies with smooth faceted surfaces, indicating that Nb is distributed

homogeneously across the TiO_2 without obvious aggregation. The exposed facets are (001) facets (the top and bottom facets), (101) facets (the isosceles trapezoids), and the additional rhombus facets with four truncated corners corresponding to the highest-surface-energy (110) facets.[41] Energy-dispersive X-ray spectroscopy (EDS) elemental mapping (Figure 4B−E) with EDS spectrum (Figure S7) revealed the uniform distribution of Nb, Ti, and O. Compared with the Nb-TiO_2 without (110) facets (Figure S8), we can confirm the presence of (110) facets and the existence of Nb in the sample.

Atomic-resolution aberration-corrected high-angle annular dark-field scanning transmission electron microscopy (HAADF-STEM) images allowed direct measurement of the lattice spacings at 0.35 and 0.24 nm (Figure 4F−H), in good agreement with the expected values of 0.351 and 0.237 nm for the (101) and (004) anatase TiO_2 lattices. As shown in Figure 4F, the angle labeled in the corresponding fast Fourier transform (FFT) image is 68°, matching well with the reference value for the expected angle between the (101) and (001) facets.[42] High magnification imaging (Figure 4H) revealed a dispersion of bright dots (indicated by circle annotations) which we attributed to individual Nb atoms on the TiO_2 support. Intensity line profiles analysis of Figure 4H supports this (Figure 4I and J); box-averaged line profiles were acquired across several of the Nb sites indicated in Figure 4H, as denoted by line annotations in Figure 4I, yielding HAADF intensity profiles (Figure 4J). The larger atomic number of Nb (Z = 41), compared to Ti (Z = 22), yielded significantly higher intensity HAADF peaks at the Nb adatom sites, as indicated by arrows in the intensity plots (Figure 4J). No Nb particles or aggregates were observed, indicating that Nb mainly existed in the form of atoms, consistent with the afore-mentioned XAFS results (Figure 3).

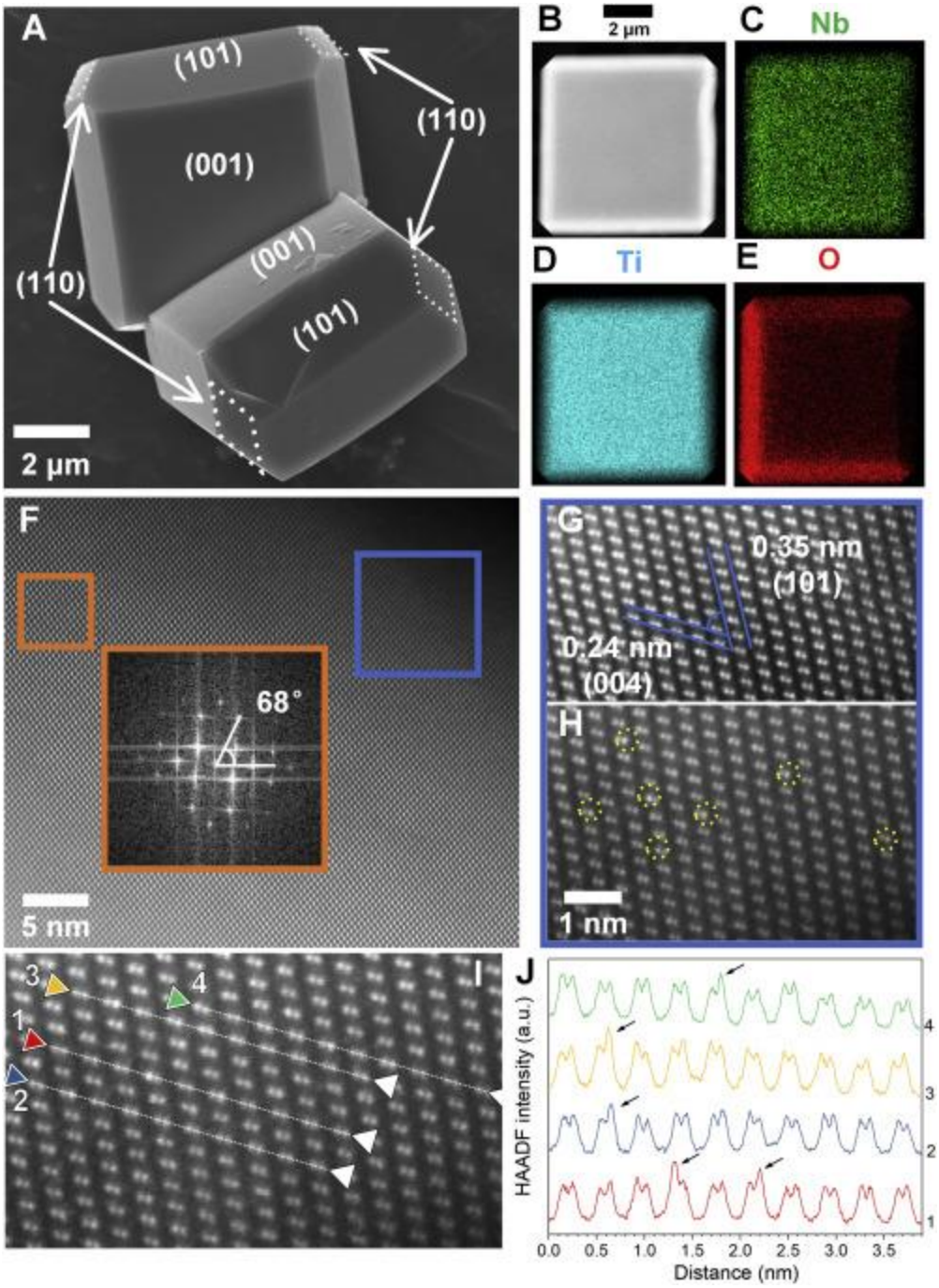

Figure 4. (A) SEM image, (B) TEM image and corresponding elemental EDS maps of (C) Nb, (D) Ti, and (E) O of 3.36% Nb-TiO_2(110). (F) HAADF-STEM image of 3.36% Nb-TiO_2(110). Inset: corresponding FFT. (G) and (H) correspond to the regions enclosed by the blue square in (F). Yellow dotted circles indicate Nb sites. (I) Box-averaged intensity line profiles acquired from

the indicated annotations (same image as (H)). (J) The intensity profiles extracted from (I), with arrows indicating Nb sites.

The NRR measurements were evaluated at ambient conditions using an H-type two-compartment cell separated by a Nafion 117 membrane. A neutral electrolyte (0.1 M Na_2SO_4 solution) was applied to overcome the corrosion problems that are common in acidic and alkaline electrolytes. All potentials for electrochemical NRR were reported on a RHE scale. In order to eliminate any possible nitrogen contaminant, N_2 with high purity (99.9999%) was used as a feeding gas without any other nitrogenous element (Figure S9), and no nitrogenous material was introduced during the catalyst preparation process, as evidenced by the EDS spectrum (Figure S7) and the high-resolution N 1s XPS spectra (Figure 2D). Before NRR measurements, the N_2 feed gas first passed through 0.1 M KOH solution to remove NO_x from the gas, then through 0.05 M H_2SO_4 solution to remove NH_3, and finally through silica gel to remove water vapor.[43] It was ensured that no NO_3^- and NO_2^- were present in the N_2-saturated electrolyte (Figures S10 and S11). After each 1 h long NRR electrolysis, the produced NH_3 was quantitatively determined by the indophenol blue method (Figure S12), ion chromatography, and ammonia/ammonium ion selective electrodes (ISE) (Figure S13). The possible presence of N_2H_4 by-product was also checked for using the Watt and Chrisp method.

The linear sweep voltammetry (LSV) curves of pristine TiO_2(110) and Nb-TiO_2(110) catalysts show increased responses for current density after changing the atmosphere from Ar to N_2 (Figure 5A), indicating that nitrogen reduction occurs on these catalysts. Moreover, Nb-TiO_2(110) exhibited a significantly higher current density than TiO_2(110), demonstrating that the Nb-TiO_2(110) catalysts are more feasible for the NRR. A series of control and blank experiments were

conducted, including in Ar-purged solution (under the exact same conditions as the NRR experiments); in the complete absence of catalyst; catalyst with just the background Nafion solution binder; holding the catalyst at an open circuit potential; and with catalyst precursor solutions. The results showed that almost no NH_3 was present in the background (Figure 5B). Cyclic voltammetry measurement showed no typical ammonia oxidation peak, which would be expected to appear at ~0.7 V (*vs*. RHE)[44] (Figure S14). These measurements exclude possible contamination from any external source except the N_2 feed gas. Moreover, the electrolyte was open in the air close to the operator for extended durations. It showed that only a negligible amount of NH_4^+ was detected after 4 h of exposure (Figure S15). This rules out impacts of environment, electrolyte, and operator on the NRR. Under reaction conditions, only NH_4^+ ions were detected, and no N_2H_4 by-product was observed (Figure S16), indicating the good selectivity of the catalysts to NH_3.

The average NH_3 yield rates and corresponding FEs of pristine TiO_2(110) and Nb-TiO_2(110) under various electrode potentials are shown in Figure 5C and D. The performance of Nb-TiO_2(110) surpassed TiO_2(110) at all applied potentials. A maximum NH_3 yield rate of ~21.3 μg h^{-1} mg_{cat}^{-1} and FE of ~9.2% were achieved at −0.5 V over Nb-TiO_2(110). The concentration of NH_4^+ was also detected by ISE and ion chromatography, which showed equivalent results to the spectrophotometric method. Isotopic labeling using $^{15}N_2$ in combination with isotope sensitive proton nuclear magnetic resonance (^{1}H NMR) was further performed. The ^{1}H NMR spectrum of the NRR product exhibited a doublet coupling (~73 Hz) typical for $^{15}NH_4^+$ compared with a triplet coupling (~52 Hz) for $^{14}NH_4^+$ (Figure S17A). The absolute dominant $^{15}NH_4^+$ doublets confirmed that the N in NH_3 stemmed from the gaseous N_2 supplied. Furthermore, we carried out quantitative NMR analysis using $^{15}N_2$ as a feed gas and obtained the signal integration-concentration linear

relation (Figure S17B and C). The $^{15}NH_3$ yield rate at −0.5 V was determined to be ~21.9 μg h^{-1} mg_{cat}^{-1}, consistent with the $^{14}NH_3$ yield rate obtained under similar conditions except using $^{14}N_2$ as a feed gas quantified by the indophenol blue method, ion chromatography, and ammonia/ammonium ion selective electrodes (ISE). This verifies the reduction of N_2 into NH_3 catalyzed by the Nb-TiO_2(110) catalyst. The NH_3 partial geometric current density on Nb-TiO_2(110) was 17.5 μA cm^{-2} at −0.5 V, nearly two times higher than that of TiO_2(110) (Figure 5E). However, the competing HER greatly reduces the NH_3 yields and FEs with increase of the applied potential below −0.5 V.

For comparison, the NRR activities of commercial anatase TiO_2, P25, pristine TiO_2 without and with (110) facets, and Nb-TiO_2 without and with (110) facets, were also evaluated under identical conditions. As displayed in Figure 5F, pristine TiO_2 exhibited a decreased NH_3 yield compared to TiO_2 with Nb loading. Specially, Nb-TiO_2(110) achieved better NRR performance than Nb-TiO_2 without exposed (110) facets. From these results, it can be deduced that the significantly boosted NRR activity of Nb-TiO_2(110) stems primarily from the synergistic effect of Nb and TiO_2(110) facets. The effect of Nb loading amount on the NRR performance was also investigated. A volcano relation was observed (Figure S18). The NRR activity increased with increasing Nb content and maximized at 3.36%, plausibly due to the increment of active atomically dispersed Nb sites. Beyond, further increasing the Nb loading led to a drop in NRR performance, likely resulting from the formation of Nb aggregates at high Nb contents. It is worth noting that Nb-TiO_2(110) surpasses most previously reported TiO_2- and Nb-based electrocatalysts in terms of NH_3 yield rate and FE (Table S2).

Tafel analysis was performed to reveal the kinetics for NH_3 formation. The Tafel slope of Nb-TiO_2(110) (~188.1 mV dec^{-1}) was substantially lower than that of pristine TiO_2(110) (~262.5 mV

dec^{-1}) (Figure 6A), indicating that Nb-loaded catalyst greatly promotes the NRR kinetics. The electrochemical active surface area (ECSA) was determined based on the electrochemical double-layer capacitance (C_{dl}). Nb-TiO_2(110) possessed a markedly higher C_{dl} compared TiO_2(110) (Figure S19), suggesting more active sites for NRR on the surface of Nb-TiO_2(110). In addition, Nyquist plots (Figure 6A) showed a lower charge transfer resistance for Nb-TiO_2(110), in accordance with its superior NRR activity.

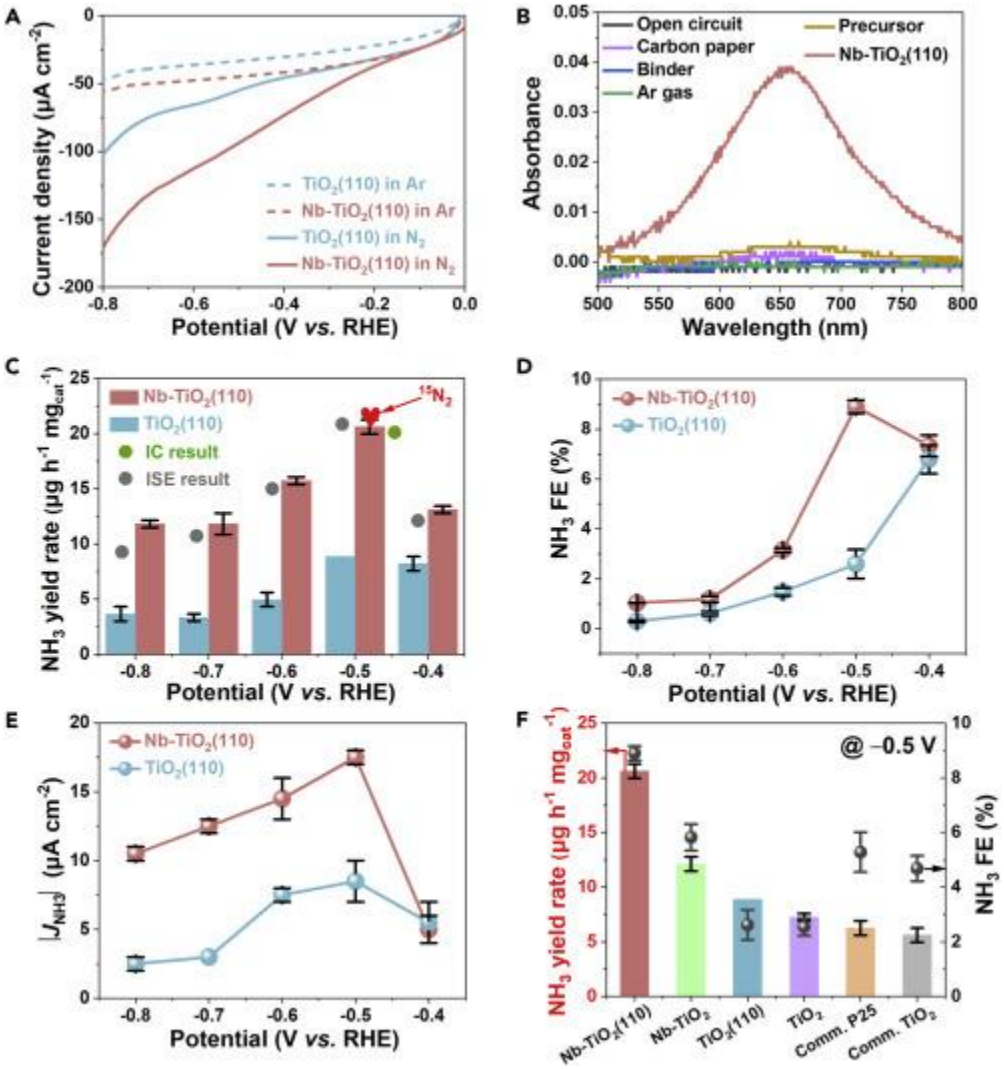

Figure 5. (A) The LSV results of TiO_2(110) and 3.36% Nb-TiO_2(110) on glassy carbon electrodes in Ar- (dashed line) or N_2 (solid line)-purged 0.1 M aqueous Na_2SO_4 with a scan rate of 5 mV s^{-1}.

(B) UV-vis absorption spectra of the electrolytes after electrolysis at −0.5 V for the control experiments with Ar-saturated electrolyte (Ar gas), or pure carbon paper, or with only the background Nafion solution (Binder), or at an open circuit (Open circuit), or with catalyst precursor solutions (Precursor). (C) The NH_3 yield rates (the heart symbol in the figure indicates the $^{15}NH_3$ yield rate determined by ^1H NMR), (D) FEs, and (E) the NH_3 partial geometric current densities at different applied potentials over TiO_2(110) and 3.36% Nb-TiO_2(110). (F) The FEs and yield rates of NH_3 over various TiO_2 catalysts at −0.5 V in N_2-saturated 0.1 M Na_2SO_4 solution.

The stability of Nb-TiO_2(110) was investigated by various assays. After alternating electrolysis between Ar and N_2-saturated electrolytes, the NH_3 formation rate and FE over Nb-TiO_2(110) were well preserved during each cycle (Figure 6C). The time-current curves performed at −0.5 V (Figure 6D) exhibited a negligible decrease in current density during a long-term electrolysis of 70 h. The NH_3 yield and FE decreased by approximately 10% after 70 h of electrolysis (inset of Figure 6D) probably due to loss of the exposed (110) facet (Figure S20). We also performed the cycle tests continuously for 10 times in N_2-saturated 0.1 M Na_2SO_4. The Nb-TiO_2(110) catalyst still maintained efficient NRR activity with nearly constant NH_3 yield rates and FEs (Figure S21), further confirming the superior repeatability and stability of the catalyst. The bulk pH of the electrolyte after 1 h of electrolysis was found to show almost no change (Figure S22), despite an apparent increase in pH after 30 h of electrolysis due to consumption of protons during the extended NRR. The effect of pH (especially local pH) change on the NRR in different types of electrolytes will be explored in our future study.

Operando Raman spectroscopy was further employed to monitor the possible reaction intermediates or products on Nb-TiO_2(110) at –0.5 V in an N_2-saturated 0.1 M Na_2SO_4 electrolyte.

In contrast to the result obtained under open circuit potential, obvious Raman modes gradually appeared as the reaction progressed (Figure 6E and F). The peaks at approximately 980, 3150, and 3300 cm^{-1}, can be assigned to NH_3[44] and N–H[45], respectively, indicating strong nitrogen reduction to NH_3 on the electrode, further confirming the calculated NRR pathway and the excellent NRR performance.

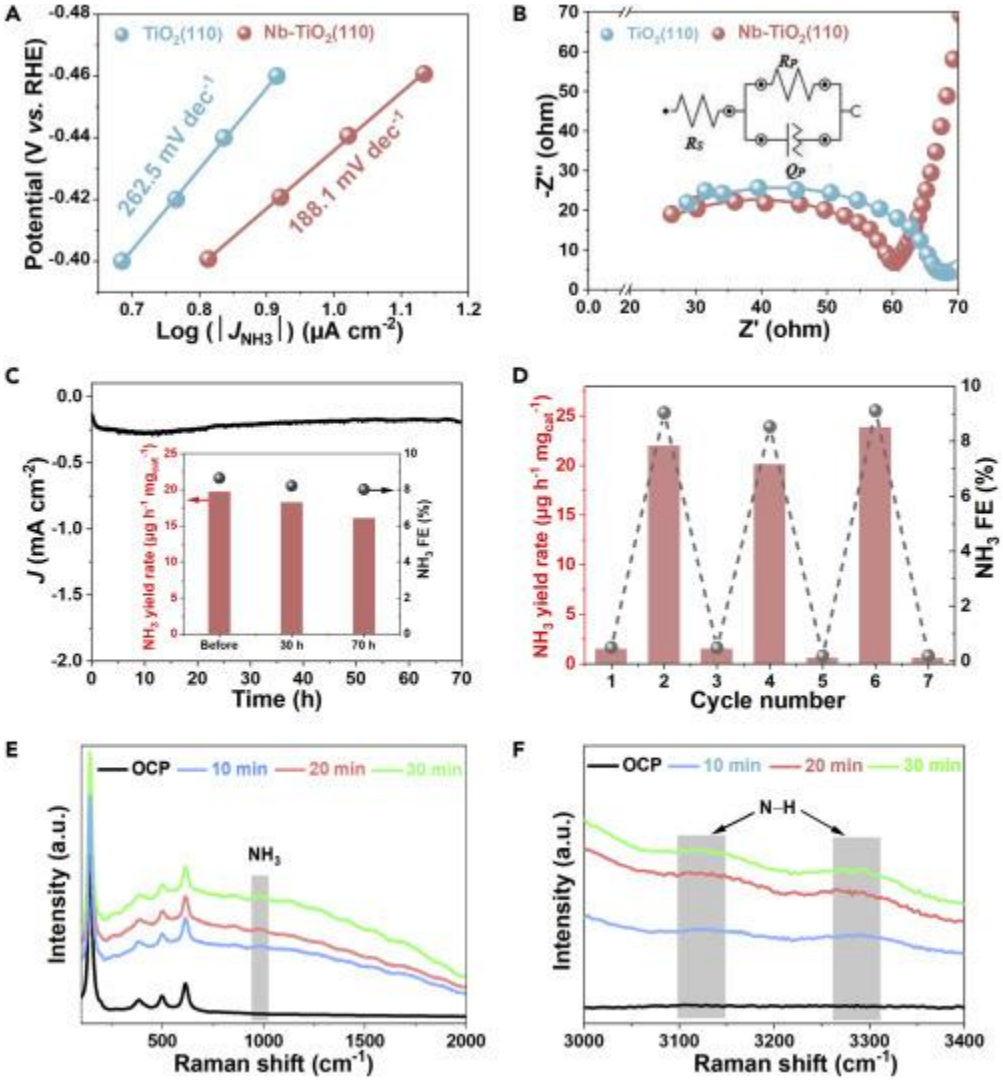

Figure 6. (A) Tafel plots and (B) EIS profiles of TiO_2(110) and 3.36% Nb-TiO_2(110). (C) The FE and yield rate for NH_3 formation over 3.36% Nb-TiO_2(110) with alternated cycles between Ar- and N_2-saturated 0.1 M Na_2SO_4 at −0.5 V. (D) Long-term durability of 70 h at −0.5 V over 3.36%

Nb-TiO_2(110) electrode. (E, F) Time-resolved operando Raman spectra of 3.36% Nb-TiO_2(110) collected at −0.5 V under open circuit potential and N_2 atmosphere at different reaction periods.

3. CONCLUSION

We predicted by DFT calculations that Nb atoms loaded on TiO_2(110) facets would be conducive to improving the stability and conductivity of TiO_2, activating the inert Ti sites for N_2 adsorption, hindering the HER activity, and reducing the energy barrier of NRR pathways. Accordingly, we successfully exposed the (110) facets of anatase TiO_2 and loaded Nb atoms, yielding a new high performance NRR electrocatalyst. Our Nb-TiO_2(110) catalyst affords a high NH_3 yield of approximately 21.3 μg h^{-1} mg_{cat}^{-1} and an FE of ~9.2% at −0.5 V in 0.1 M Na_2SO_4, with a long-term stability of 70 h. The performance of Nb-TiO_2(110) exceeds most previously reported TiO_2- and Nb-based electrocatalysts for NRR at ambient conditions. This work provides a protocol for the rational design and development of highly efficient metal electrocatalysts for electrochemical N_2 fixation.

AUTHOR CONTRIBUTIONS

Z. S. and X. T. supervised the project. Z. S. and Y. G. conceived the idea. Y. G. conducted synthesis and electrochemical experiments. S. H. and A. W. R. performed transmission electron microscopy measurements and analysis. Q. Y helped conduct $^{15}N_2$ isotope analysis. Y. Y. made DFT calculations. Z. S., X. T., L. H., and Y. G. wrote the manuscript. A. W. R. polished the language. All authors reviewed the manuscript.

DECLARATION OF INTERESTS

The authors declare no competing financial interest.

ACKNOWLEDGMENT

This work was supported by the National Natural Science Foundation of China (No. 21972010) and Beijing Natural Science Foundation (No. 2192039). The calculation data in this paper were supported by high performance computing platform of BUCT.

REFERENCES

(1) Shen, H., Choi, C., Masa, J., Li, X., Qiu, J., Jung, Y., and Sun, Z. (2021). Electrochemical ammonia synthesis: mechanistic understanding and catalyst design. Chem *7*, 1708−1754.

(2) Rösch, B. Gentner, T.X., Langer, J., Färber, C., Eyselein, J., Zhao, L., Harder, S. (2021). Dinitrogen complexation and reduction at low-valent calcium. Science *371*, 1125−1128.

(3) Smith, C., Hill, A. K., Torrente-Murciano, L. (2020). Current and future role of Haber–Bosch ammonia in a carbon-free energy landscape. Energ. Environ. Sci. *13*, 331−344.

(4) Chen, J. G., Crooks, R. M., Seefeldt, L. C., Bren, K. L., Bullock, R. M., Darensbourg, M. Y., Holland, P. L., Hoffman, B., Janik M. J., Jones, A. K., Kanatzidis, M. G., King P., Lancaster K. M., Lymar, S. V., Pfromm, P., Schneider, W. F., Schrock, R. R. (2018). Beyond fossil fuel-driven nitrogen transformations. Science *360*, 6391.

(5) Prabhu, P., Jose, V., Lee, J. M. (2020). Design strategies for development of TMD-based heterostructures in electrochemical energy systems. Matter *2* 526−553.

(6) Wang, H., Li, J., Li, K., Lin, Y., Chen, J., Gao, L., Xu, X., Lee, J. M. (2021). Transition metal nitrides for electrochemical energy applications. Chem. Soc. Rev. *50*, 1354−1390.

(7) Soloveichik, G. (2019). Electrochemical synthesis of ammonia as a potential alternative to the Haber-Bosch process. Nat. Catal. *2*, 377−380.

(8) Wang, H., Chen, J., Lin, Y., Wang, X., Li, J., Li, Y., Chao, D., Xu, X., Lee, J. M. (2021). Electronic modulation of non-van der Waals 2D electrocatalysts for efficient energy conversion. Adv. Mater. *33*, 2008422.

(9) Qing, G., Ghazfar, R., Jackowski, S.T., Habibzadeh, F., Ashtiani, M.M., Chen, C.P., Hamann, T.W. (2020). Recent advances and challenges of electrocatalytic N_2 reduction to ammonia. Chem. Rev. *120*, 5437−5516.

(10) Prabhu, P., Lee, J. M. (2021). Metallenes as functional materials in electrocatalysis. Chem. Soc. Rev. *50*, 6700-6719.

(11) Tao, H., Choi, C., Ding, L.X., Jiang, Z., Han, Z., Jia, M., Sun, Z. (2019). Nitrogen fixation by Ru single-atom electrocatalytic reduction. Chem *5*, 204–214.

(12) Zhang, M., Choi, C., Huo, R., Gu, G.H., Hong, S., Yan, C., Sun, Z. (2020). Reduced graphene oxides with engineered defects enable efficient electrochemical reduction of dinitrogen to ammonia in wide pH range. Nano Energy *68*, 104323.

(13) Ren, Y., Yu, C., Tan, X., Huang, H., Wei, Q., Qiu, J. (2021). Strategies to suppress hydrogen evolution for highly selective electrocatalytic nitrogen reduction: challenges and perspectives. Energy Environ. Sci. *14*, 1176−1193.

(14) Guo, Y., Gu, J., Zhang, R., Zhang, S., Li, Z., Zhao, Y., Zhi, C. (2021). Molecular crowding effect in aqueous electrolytes to suppress hydrogen reduction reaction and enhance electrochemical nitrogen reduction. Adv. Energy Mater. *11*, 2101699

(15) Zhang, J., Yang, L., Wang, H., Zhu, G., Wen, H., Feng, H., Yao, Y. (2019). In situ hydrothermal growth of TiO_2 nanoparticles on a conductive $Ti_3C_2T_x$ MXene nanosheet: a synergistically active Ti-based nanohybrid electrocatalyst for enhanced N_2 reduction to NH_3 at ambient conditions. Inorg. Chem. *58*, 5414−5418.

(16) Zhang, R., Ren, X., Shi, X., Xie, F., Zheng, B., Guo, X., Sun, X. (2018). Enabling effective electrocatalytic N_2 conversion to NH_3 by the TiO_2 nanosheets array under ambient conditions. ACS Appl. Mater. Inter. *10*, 28251−28255

(17) Han, Z., Choi, C., Hong, S., Wu, T.S., Soo, Y.L., Jung, Y., Sun, Z. (2019). Activated TiO_2 with tuned vacancy for efficient electrochemical nitrogen reduction. Appl. Catal. B Environ. *257*, 117896.

(18) Wu, T., Kong, W., Zhang, Y., Xing, Z., Zhao, J., Wang, T., Sun, X. (2019). Greatly enhanced electrocatalytic N_2 reduction on TiO_2 via V doping. Small Methods *3*, 1900356.

(19) Wu, T., Zhu, X., Xing, Z., Mou, S., Li, C., Qiao, Y., Sun, X. (2019). Greatly improving electrochemical N_2 reduction over TiO_2 nanoparticles by iron doping. Angew. Chem. Int. Ed. *58*, 18449−18453.

(20) Cao, N., Chen, Z., Zang, K., Xu, J., Zhong, J., Luo, J., Zheng, G. (2019). Doping strain induced bi-Ti^{3+} pairs for efficient N_2 activation and electrocatalytic fixation. Nat. Commun. *10*, 1−12.

(21) Wu, T.; Zhao, H.; Zhu, X.; Xing, Z.; Liu, Q.; Liu, T.; Sun, X. (2020). Identifying the origin of Ti^{3+} activity toward enhanced electrocatalytic N_2 reduction over TiO_2 nanoparticles modulated by mixed-valent copper. Adv. Mater. *32*, 2000299.

(22) Li, L., Chen, H., Li, L., Li, B., Wu, Q., Cui, C., Sun, X. (2021). La-doped TiO_2 nanorods toward boosted electrocatalytic N_2-to-NH_3 conversion at ambient conditions. Chin. J. Catal. *42*, 1755−1762.

(23) Pan, J., Liu, G., Lu, G. Q., Cheng, H.M. (2011). On the true photoreactivity order of {001}, {010}, and {101} facets of anatase TiO_2 crystals. Angew. Chem. Int. Ed. *50*, 2133−2137.

(24) Liu, G., Niu, P., Sun, C., Smith, S.C., Chen, Z., Lu, G.Q., Cheng, H.M. (2010). Unique electronic structure induced high photoreactivity of sulfur-doped graphitic C_3N_4. J. Am. Chem. Soc. *132*, 11642−11648.

(25) Diebold, U. (2003). The Surface Sience of Titanium Dioxide. Surf. Sci. Rep. *48*, 53−229.

(26) Jose, V., Nsanzimana, J. M. V., Hu, H., Choi, J., Wang, X., Lee, J. M. (2021). Highly efficient oxygen reduction reaction activity of N-doped carbon–cobalt boride heterointerfaces. Adv. Energy Mater. *11*, 2100157.

(27) Chu, K., Liu, Y.P., Li, Y.B., Guo, Y.L., Tian, Y., Zhang, H. (2020). Multi-functional Mo-doping in MnO_2 nanoflowers toward efficient and robust electrocatalytic nitrogen fixation. Appl. Catal. B Environ. *264*, 118525.

(28) Zhang, Z., Xu, X. (2020). Efficient Heteronuclear Diatom Electrocatalyst for Nitrogen Reduction Reaction: Pd-Nb Diatom Supported on Black Phosphorus. ACS Appl. Mater. Inter. *12*, 56987−56994.

(29) Yang, T., Song, T.T., Zhou, J., Wang, S., Chi, D., Shen, L., Feng, Y.P. (2020). High-throughput screening of transition metal single atom catalysts anchored on molybdenum disulfide for nitrogen fixation. Nano Energy *68*, 104304.

(30) Maintz, S., Deringer, V.L., Tchougréeff, A.L., Dronskowski, R. (2016). LOBSTER: A tool to extract chemical bonding from plane-wave based DFT. J. Comput. Chem. *37*, 1030−1035.

(31) Ren, X., Zhao, J., Wei, Q., Ma, Y., Guo, H., Liu, Q., Wang, Y., Cui, G., Asiri, A.M., Li, B., Tang, B., Sun, X. (2019). High-performance N_2-to-NH_3 conversion electrocatalyzed by Mo_2C nanorod. ACS Cent. Sci. *5*, 116−121.

(32) Kong, W., Liu, Z., Han, J., Xia, L., Wang, Y., Liu, Q., Sun, X. (2019). Ambient electrochemical N_2-to-NH_3 fixation enabled by Nb_2O_5 nanowire array. Inorg. Chem. Front. *6*, 423−427.

(33) Uekawa, N., Watanabe, M., Kaneko, K., Mizukami, F. (1995). Mixed-valence formation in highly oriented Ti-doped iron oxide film. J. Chem. Soc. Faraday Trans. *91*, 2161.

(34) Moses, P.R., Wier, L.M., Lennox, J.C., Finklea, H.O., Lenhard, J.R., Murray, R.W. (1978). X-ray photoelectron spectroscopy of alkylaminesilanes bound to metal oxide electrodes. Anal. Chem. *50*, 576−585.

(35) Wang, D.H., Jia, L., Wu, X.L., Lu, L.Q., Xu, A.W. (2012). One-step hydrothermal synthesis of N-doped TiO_2/C nanocomposites with high visible light photocatalytic activity. Nanoscale **2012** *4*, 576−584.

(36) Uwamino, Y., Ishizuka, T., Yamatera, H. (1984). X-ray photoelectron spectroscopy of rare-earth compounds. J. Electron Spectrosc. *34*, 67−78.

(37) Ohsaka, T., Izumi, F., Fujiki, Y. (1978). Raman spectrum of anatase, TiO_2. J. Raman Spectrosc. *7*, 321−324.

(38) Middleton, A.P., Edwards, H.G.M., Middleton, P.S., Ambers, J. (2005). Identification of anatase in archaeological materials by Raman spectroscopy: implications and interpretation. J. Raman Spectrosc. *36*, 984−987.

(39) León, A., Reuquen, P., Garín, C., Segura, R., Vargas, P., Zapata, P, Orihuela, P.A. (2017). FTIR and Raman characterization of TiO_2 nanoparticles coated with polyethylene glycol as carrier for 2-methoxyestradiol. Appl. Sci. *7*, 49−58.

(40) Liu, Q., Ai, L., Jiang, J. (2018). MXene-derived TiO_2@C/gC_3N_4 heterojunctions for highly efficient nitrogen photofixation. J. Mater. Chem. A *6*, 4102−4110.

(41) Liu, M., Piao, L., Zhao, L., Ju, S., Yan, Z., He, T., Wang, W. (2010). Anatase TiO_2 single crystals with exposed {001} and {110} facets: facile synthesis and enhanced photocatalysis. Chem. Commun. *46*, 1664−1666

(42) Dai, Y., Cobley, C.M., Zeng, J., Sun, Y., Xia, Y. (2009). Synthesis of anatase TiO_2 nanocrystals with exposed {001} facets. Nano Lett. *9*, 2455−2459.

(43) Gao, L.F., Cao, Y., Wang, C., Yu, X.W., Li, W.B., Zhou, Y., Zou, Z.G. (2021). Domino effect: gold electrocatalyzing lithium reduction to accelerate nitrogen fixation. Angew. Chem. Int. Ed. *60*, 5257−5261.

(44) Ziegler, L.D., Hudson, B. (1984). Resonance rovibronic Raman scattering of ammonia. J. Phys. Chem. *88*, 1110–1116.

(45) Zhao, Y., Li, F., Li, W., Li, Y., Liu, C., Zhao, Z., Shan, Y., Ji, Y., Sun, L. (2021). Identification of M-NH_2-

NH_2 intermediate and rate determining step for nitrogen reduction with bioinspired sulfur-bonded FeW catalyst. Angew. Chem. Int. Ed. *60*, 20331−20341.